IEEE Access
Multidisciplinary | Rapid Review | Open Access Journal

Received December 3, 2020, accepted December 10, 2020, date of publication December 15, 2020,
date of current version December 30, 2020.

Digital Object Identifier 10.1109/ACCESS.2020.3044908

Narrow-Beam Antenna for Short-Distance Non-Destructive Sensor in Fruit-Ripeness Monitoring

HOANG NAM DAO, (Member, IEEE), CHUWONG PHONGCHAROENPANICH, (Member, IEEE), AND MONAI KRAIRIKSH, (Senior Member, IEEE)
Department of Telecommunications Engineering, School of Engineering, King Mongkut's Institute of Technology Ladkrabang, Bangkok 10520, Thailand
Corresponding author: Monai Krairiksh (monai.kr@kmitl.ac.th)

This work was supported in part by the King Mongkut's Institute of Technology Ladkrabang under Grant KDS2019/001 and in part by the U.S. Office of Naval Research Global under Grant N62909-18-1-2047.

ABSTRACT Radiation pattern subtraction is a useful technique for narrowing a receiving antenna's radiation pattern in a short-distance, non-destructive sensor. The sensor's antenna was developed to be compact and light-weight as well as to operate in real-time. This work applied the principle of radiation pattern subtraction to narrow the beamwidth of an antenna. Our experimental data demonstrated that a simple narrow-beam three-element antenna with a 35° half-power beamwidth and a small size of 5.9×6.5 cm^2 could be realized. In the experiment, the radiation pattern of an array antenna (consisting of two halfwave dipoles with a reflector) was subtracted from the radiation pattern of an element antenna (consisting of a halfwave dipole with a reflector) for the three-element antenna to achieve a narrow beamwidth and compact size. The antenna had a simple feeding network that operated at 10.525 GHz and 35° half-power beamwidth. The angular resolution of the receiving antenna was tested with mango fruits: it was able to resolve an 80 mm separation between the fruit of interest and the nearby fruit, which was sufficient, in terms of practicality, for mitigating the interfering effect of nearby fruits to the fruit of interest. This type of antenna is useful as a short-distance, non-destructive sensor such as a pre-harvest sensor.

INDEX TERMS Pre-harvest sensor, short-distance, non-destructive sensor, angular resolution improvement, radiation pattern subtraction, dipole array, far-field phase distribution, top-load dipole.

I. INTRODUCTION

Recently, the United Nations (UN) has announced 17 sustainable development goals (SDG) to make the world free of poverty, hunger, and disease [1]. The 12th sustainable development goal (SDG12) mandates responsible and sustainable food consumption and production. Producers must be able to grow more food while reducing negative environmental impacts. Consumers must be encouraged to shift to a nutritious and safe diet with a low environmental footprint. In the sense of global food security, increasing production through the addition of more production areas is not sustainable. On the other hand, increasing productivity per unit of land is sustainable. For fruit production, the timing of harvest is critical. Over or under-ripe fruits have low or no retail value and are considered a loss or waste of resources. For consumers, fruits harvested too early would have low quality and unacceptable taste. Fruits harvested too late have a short shelf life, poor appearance, and an "off" flavor and odor. In-field assessment of fruit ripeness with an accurate prediction of both the harvest date and yield can significantly reduce waste in the supply chain in the addition to improve food security. To predict an optimal harvest date, a non-destructive technique (to the fruits) for determining the exact ripening date is necessary [2]. The ripening stage can be predicted as well as the rate of ripening that depends on environmental factors.

Numerous modern sensor technologies in fruit harvesting have been developed. Computer vision and proximity sensors (non-vision) can detect spatial features of plants and fruits. They can be used for plant inspection, determination of fruit size and shape, insect detection, and firmness measurement. Ripening stage can also be estimated by computer vision, chemical sensor, and spectroscopy [3]. Computer vision and

The associate editor coordinating the review of this manuscript and approving it for publication was Di Zhang.

chemical sensors have severe limitations of interference from sunlight and the concentrated gas in the closed detection system. Microwave technology that is oblivious to these kinds of interference is a better candidate for the task. Microwave radar at S-band has been developed to estimate grape production yield in the wine industry [4]. It was useful for logistics and supply chain management. The sugar content of apples can be estimated with a millimeter-wave reflectometer [5]. The estimated results from a reflectometer calibrated by an artificial neural network were entirely accurate. The natural frequencies of thick-peel fruits can be determined from a radar cross-section at L-band by the Cauchy method [6]. As the dielectric property of fruit flesh varies with time during the ripening process, its natural frequency can be used to predict a suitable harvest date. Those previously mentioned papers are some fruit classification applications of non-destructive sensors that measure the radar cross-section (RCS) of a target at a short distance. It is a feasible pre-harvest fruit sensor technology since the RCS of fruit changes with passing days [7]. However, if the sensor antenna's beamwidth is too wide, the angular resolution (the minimum angular separation at which two equal-sized targets can be separated when they are placed at the same distance from the sensor [8]) will be too low. In other words, measurement results from a sensor with too broad beamwidth will be too prone to errors due to nearby fruits' presence. Angular resolution characteristics are determined by antenna beamwidth, which is represented by a half-power point (-3 dB) angle. It is necessary to improve the pre-harvest sensor's angular resolution to obtain the most accurate hence the most reasonable estimates.

Generally, a narrow beamwidth can be achieved from a large aperture antenna that requires a sizeable far-field range for the plane wave to impinge on the target. It can operate in long-range. One of the attractive approaches that can accomplish a compact size sensor antenna is an approach that uses radiation pattern subtraction, previously applied in radiation pattern measurement field [9], [10]. Recently, it was applied to improve the spatial resolution of an ultrasonic imaging system [11]. Nevertheless, the phase was not taken into account. Sakogawa *et al.* [12] presented a beam subtraction scheme to tighten the RFID sensor's beamwidth for a security system. Their work employed hybrid couplers to perform radiation pattern subtraction, and the antenna structure was accomplished for a monopulse procedure. The application of interest was a sensor in a shoplifting warning system.

We presented a technique to narrow down beamwidth by subtracting two different radiation patterns. The developed antenna system was intended to be used as a pre-harvest fruit sensor [13].

Such an antenna needs a memory unit and a signal processing unit. However, the radiation pattern subtraction antenna would be done with a suitable feeding network to remove the need for memory and signal processing unit. The antenna would be operating at 10.525 GHz. It was designed to be compact and light-weight so that it could be installed on a drone. To our best knowledge, there has not been any recent work focusing on the investigation of radiation pattern subtraction related to far-field phase distribution of antenna. This article presents the details of the principle of radiation pattern subtraction that had led to the simple design and implementation. This work's contributions are a wholly derived set of far-field equations from the radiation pattern subtraction principle, applied to such kind of antenna mentioned above, and a practical and straightforward antenna as a pre-harvest sensor. That set of equations allowed us to determine the feasibility of achieving narrow beamwidth by subtracting array antennas' radiation patterns. Instead of switching between two array antennas' radiation patterns and memorizing each pattern for subtraction, a feeding network was introduced so that the antenna would be compact and light-weight.

The rest of this article is organized as follows. Section II presents a problem statement of the effect of a nearby fruit on the measured RCS of the fruit of interest and the sensor antenna's desirable characteristics. Section III describes the principle of radiation pattern subtraction related to far-field phase distribution. The design and experiments on the antenna characteristics, as well as its performance in eliminating the effect of nearby fruit, are described in section IV. Finally, the conclusion is drawn in section V.

II. DESIRABLE CHARACTERISTICS OF AN ANTENNA FOR SHORT-DISTANCE, NON-DESTRUCTIVE, FRUIT-RIPENESS MONITORING SENSOR

When a nearby fruit is sufficiently far away from the fruit of interest, the problem of scattered waves from such fruit is negligibly small. However, when a nearby fruit is located in close contact with the fruit of interest, the back-scattered wave from the nearby fruit will alter the fruit of interest's measurement result. Therefore, the beamwidth of the sensor's antenna must be sufficiently narrow. Fig. 1(a) shows a scenario of mango fruits (Mangifera indica) on a tree. It can be seen in the diagram in Fig. 1 (b) that the angle α_s is measured from the direction pointing to the fruit of interest to that pointing to the nearby fruit, which is d_s apart. Mango fruit is assumed to have an ellipsoidal shape. If the nearby fruit is in contact with the fruit of interest ($d = d_0$), the angle between the centers of the two fruits is α_0. The distance between the sensor and the fruit of interest (r) is in the far-field range of the sensor's antenna ($r \geq 2D^2/\lambda$), where D is the largest dimension of the sensor's antenna and λ is the wavelength at the operating frequency.

The intended sensor operates as a monostatic radar. A detected mango's radar cross-section (RCS : σ) is determined in terms of gains of transmitting and receiving antennas, power of the transmitter and the receiver, and distance between the sensor and the mango (r) [8].

Naturally, fruits of the same age have the same size and dielectric properties; hence it is reasonable to assume that they have the same RCS. Fig. 1 (b) shows that $r^{-1} = \tan\alpha_s/d_s = \tan\alpha_0/d_0$. The nearby fruit's scattered wave power is required to be less than 10% of that of the fruit of interest to limit the interfering RCS of the nearby fruit. For a

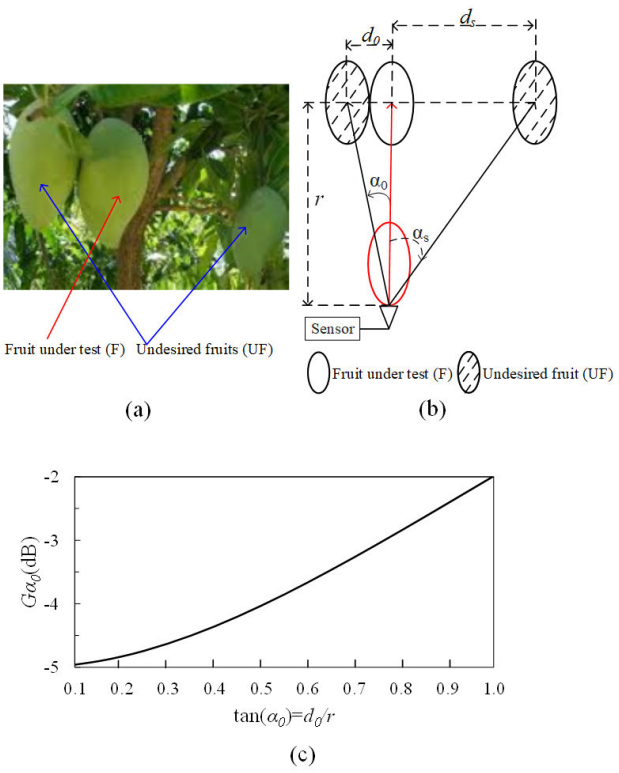

FIGURE 1. A scenario of mango fruits on a tree (a) Photograph (b) Diagram (c) Required normalized gain in the direction α_0.

short-distance microwave sensor application, the separation (d_s) between the fruit of interest and the nearby fruit can be comparable to the distance (r) between the sensor system and the fruit of interest (I). Therefore, the received power from the nearby fruit (N) not only depends upon the beamwidths of the transmitting and the receiving antennas, but also upon the angle (α_s).

From the monostatic radar equation and assuming that both the transmitter and the receiver have the same kind of antenna, the ratio of the received powers from the nearby fruit (P_N) to the fruit of interest (P_I) is given by,

$$\frac{P_N}{P_I} = \frac{G_{t\alpha_s} G_{r\alpha_s}}{G_{to} G_{ro}} \cos^4 \alpha_s = G_{\alpha_s}^2 \cos^4 \alpha_s, \tag{1}$$

where $G_{t\alpha_s}, G_{r\alpha_s}$ are the gains of the transmitting antenna and the receiving antenna in the direction α_s, respectively; G_{to}, G_{ro} are the maximum gains of the transmitting antenna and the receiving antenna, respectively; $G_{t\alpha_s}/G_{to} = G_{r\alpha_s}/G_{ro} = G_{\alpha_s}$ are the normalized gains of the transmitting and receiving antennas in the direction α_s, respectively.

For the nearby fruit located in the direction α_0,

$$2G_{\alpha_0}[\text{dB}] + 40 \log_{10} (\cos \alpha_0) = -10[\text{dB}], \tag{2}$$

where $G_{\alpha o}$ is the normalized gain of the sensor's antenna in the direction α_0.

The standard size of mango is the parameter that controls the value of the distance (d_0). The far-field range of the sensor's antenna controls the minimum distance (r) that the sensor can be placed far away from the mango of interest. The angle (α_0) between the mango centers (the mango of interest and a nearby mango) can be calculated as ($\tan \alpha_0 = d_0/r$), and the normalized gain of the sensor's antenna is required to satisfy (2) as depicted in Fig. 1 (c). The figure shows the relationship between the required normalized gain of the sensor's antennas and the angle α_0. A reduction in the maximum dimension of the sensor's antenna is equivalent to an increase in d_0/r for a fixed distance, d_0. It also means that the smaller size antenna can provide a larger angle $\alpha_0(\alpha_0 = \tan^{-1}(d_0/r))$. The required normalized gain of the sensor's antenna at the angle α_0 was calculated in (2), as depicted in Fig. 1(c). For the increasing d_0/r(ranging from 0.1 to 1.0), the term "$40 \log_{10} (\cos \alpha_0)$" in (2) decreases, and the antenna's required normalized gain increases from -5dB to $-$ 2dB. The antenna design can start with a fixed angle α_0(the fixed distance d_0 and the fixed range r); the required normalized gain of this antenna was calculated in (2), and the antenna's maximum dimension (D) was limited to $D \leq \sqrt{\lambda r/2}$.

In practice, a standard mango size is determined by the average weight, length, and width of a batch of mangoes. The standard length and width of exported mangoes are 18 cm and 8cm, respectively [14]. Therefore, the distance (d_0) is fixed at 8cm. A drone equipped with the sensor system can approach as close as 25 cm to a mango fruit on a tree. The microwave sensor system developed in this work operated at 10.525 GHz. The normalized gain of the sensor's antenna at the angle $\alpha_0 = \arctan(d_0/r) = \arctan(8/25) = 17.7°$ (from Eq. (2)), $G_{\alpha o}$, must be less than or equal to -4.57 dB. Since the microwave sensor system's operating range was $r = 25$ cm, the far-field region of the sensor's antenna $(r \geq 2D^2/\lambda)$ must be less than 25 cm. Hence, the maximum dimension of the sensor's antenna (D) must not exceed 6 cm. Finally, the beamwidth of this antenna at the -4.57 dB point must not exceed 35.4°.

III. ANALYSIS OF RADIATION PATTERN SUBTRACTION ANTENNA

For a compact size antenna, beamwidth narrowing by radiation pattern subtraction can be explained by considering the case of two linear uniform arrays that have the same kind of element and same phase center, shown in Fig. 2 (a). The desired radiation patterns of the array antenna #1 and the array antenna #2 can be generated by setting appropriate values for the parameters (d_1, β_1) and (d_2, β_2), respectively. Illustrated in Fig. 2 (a), the received electric field intensities at array antenna 1 (output of power combiner #1) and array antenna 2 (output of power combiner #2) were combined at the power combiner #3 where the inputs were designed to be out-of-phase. The array antennas #1 and #2 utilized in this work are shown in Fig. 2 (b). They were two-element array antennas of which each element was a halfwave dipole with a reflector. The electric field intensity of the array antenna can be calculated by the pattern multiplication principle shown

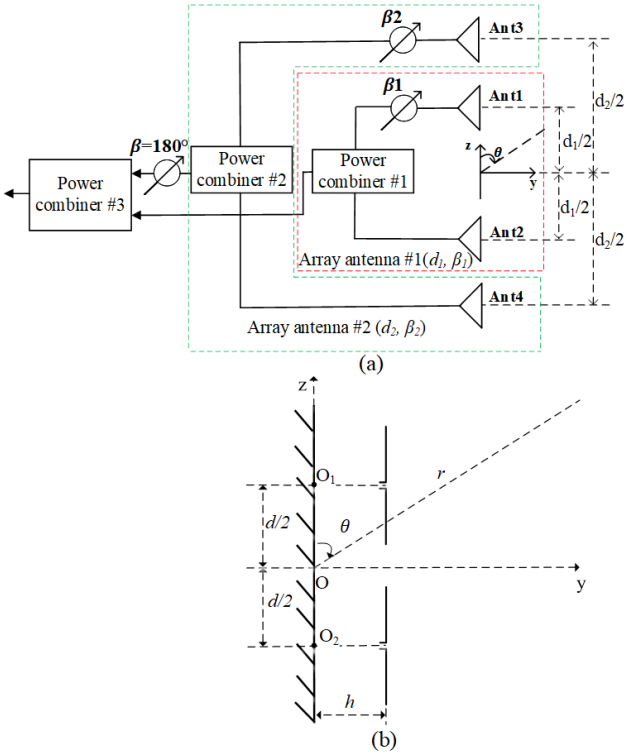

FIGURE 2. Antenna structure: (a) Architecture for radiation pattern subtraction (b) Two-element array of which element is a dipole with a reflector.

in [15]. To achieve the end-fire radiation pattern of a halfwave dipole with a reflector, the distance (h) was set to $\lambda/4$.

One obtains the radiation pattern from Eq. (3), (4), and (5)

$$E_\theta = \left[j\eta \frac{I_0 e^{-jkr}}{2\pi r} \left(\frac{\cos\left(\frac{\pi}{2}\cos\theta\right)}{\sin\theta} \right) \right] \left[2j \sin\left(\frac{\pi}{2}\sin\theta\right) \right] \times \left[2\cos\left(\frac{1}{2}(kd\cos\theta + \beta)\right) \right], \quad (3)$$

$$E_\theta = E_0 e^{j\psi} = E_0 e^{j(\psi_e + \varphi)}, \quad (4)$$

$$E_\theta = \left| \frac{2I_0}{\pi r} \left[\frac{\cos\left(\frac{\pi}{2}\cos\theta\right)}{\sin\theta} \right] \left[\sin\left(\frac{\pi}{2}\sin\theta\right) \right] \times \left[\cos\left(\frac{kd}{2}\cos\theta + \frac{\beta}{2}\right) \right] \right|, \quad (5)$$

where h is the distance between the halfwave dipole to the reflector, and d, β are the distance and phase shift between the two elements, respectively. The first square bracket in (3) represents the radiation pattern of a halfwave dipole. Those in the second and third square brackets are the contributions from the reflector and the two-element array antenna, respectively.

The far-field phase of the halfwave dipole with a reflector can be calculated from the far-field phase of the halfwave dipole element ($\psi_d = -kr + \pi/2$) located at the physical array center,

$$\psi_e = -kr + \pi \quad \text{for } 0 \le \theta \le \pi. \quad (6)$$

Equation (3) shows that the far-field phase of the two-element array is in-phase ($\psi = \psi_e$) with the far-field phase of the halfwave dipole with a reflector provided that the array factor $AF = 2\cos\left(\frac{1}{2}(kd\cos\theta) + \beta\right) > 0$. When the array and the element are out-of-phase, ($\psi = \psi_e + \pi$), the array factor $AF < 0$.

Subtraction of the radiation patterns of the two array antennas was accomplished by subtracting the respective real and imaginary parts of their electric field intensities. Hence, the far-field phase distribution was the main contributor, and the subtraction result was a magnitude subtraction for in-phase directions and magnitude summation for out-of-phase directions. The real and imaginary parts of the electric field are presented below,

$$\mathrm{Re}\,(E_\theta) = E_0 \cos\,(\psi_e + \varphi)\,, \quad (7)$$

$$\mathrm{Im}\,(E_\theta) = E_0 \sin\,(\psi_e + \varphi)\,, \quad (8)$$

where φ is the phase shift between the array and its element, calculated by,

$$\varphi = \begin{cases} 0 & \text{for } \cos\theta \in \left(\frac{-\pi - \beta}{kd}, \frac{\pi - \beta}{kd} \right) \\ \pi & \text{for } \cos\theta \notin \left(\frac{-\pi - \beta}{kd}, \frac{\pi - \beta}{kd} \right). \end{cases} \quad (9)$$

Eq. (9) indicates that the far-field phase of the two-element array varies with the distance (d) and phase shift (β) between the two elements. For a fixed phase shift (β) , as the distance increased from $kd < \beta - \pi$ to $kd < \pi - \beta$, to $|\pi - \beta| < kd < \pi + \beta$, and to $kd > \pi + \beta$, the far-field phase of the array changed from being out-of-phase to being in-phase with the far-field phase of the element in every direction. As the distance increased further, the far-field phase of the array kept changing to be in-phase in some directions and out-of-phase in some other directions. The beamwidth narrowing of the array antenna could be, therefore, achieved by increasing the distance (d).

Similarly, for a fixed distance (d), the same result could be obtained by changing the phase shift from $\beta > kd + \pi$ to $\beta < \pi - kd$ to $|\pi - kd| < \beta < \pi + kd$, and $\beta < kd - \pi$.

The radiation pattern subtraction was accomplished by subtracting the radiation pattern of array #2 ($d_2, \beta_2 = \beta$) from the radiation pattern of array #1($d_1 < d_2, \beta_1 = 0$), and the phase shift (β) was fixed at 45°.

The following four cases demonstrate possible design scenarios for a compact-size, narrow-beamwidth antenna.

Case 1: The array antenna #1 with $(d_1 = 3\lambda/8, \beta_1 = 0)$ and the array antenna #2 with $(d_2 = \lambda/2, \beta_2 = 45°)$ would be utilized for radiation pattern subtraction.

Computed from the far-field phase distribution of the array antennas, the results of the radiation pattern subtraction were a complex summation of the electric field produced by the two array antennas in the direction $0 \le \theta < 41°$ and a complex subtraction in the direction $41° \le \theta < 180°$. Since the magnitudes of the electric fields of the array antennas were much different in the direction of $40° - 90°$ and almost

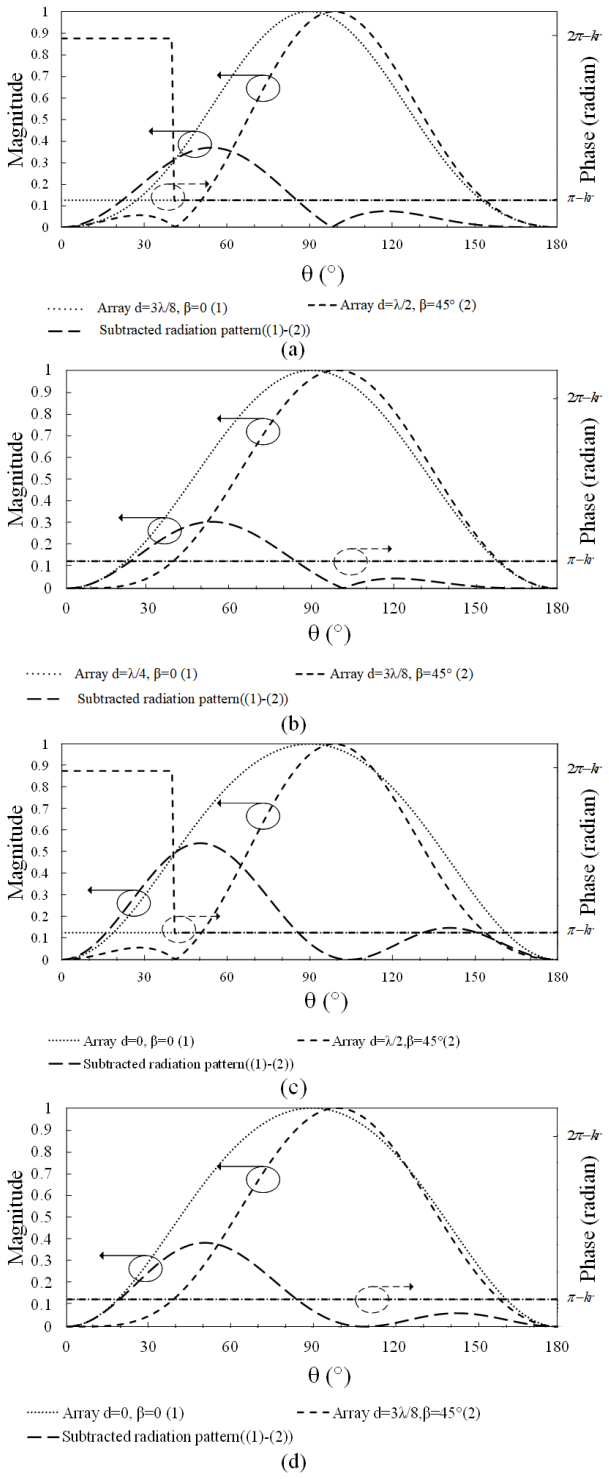

FIGURE 3. Far-field magnitude and phase distribution. (a) Array ($d = 3\lambda/8, \beta = 0$)- Array($d = \lambda/2, \beta = 45°$) (b) Array ($d = \lambda/4, \beta = 0$) - Array ($d = 3\lambda/8, \beta = 45°$) (c) Array ($d = 0, \beta = 0$) - Array($d = \lambda/2, \beta = 45°$) (d) Array ($d = 0, \beta = 0$) - Array ($d = 3\lambda/8, \beta = 45°$).

identical in the direction of $100° - 170°$, the subtracted radiation pattern had a main beam in the direction of 54° and a sidelobe in the direction of 117° as depicted in Fig. 3 (a). The half-power beam width (HPBW) of the subtracted radiation pattern was 38.3°. The sidelobe level was −13.9 dB.

Case 2: For a shorter distance between elements, the sizes of array antenna #1 with $(d_1 = \lambda/4,\ \beta_1 = 0)$ and array antenna #2 with $(d_2 = 3\lambda/8,\ \beta_2 = 45°)$ can be reduced. Fig.3 (b) indicates that the far-field phases of the two array antennas are in-phase in every direction, so the results of the radiation pattern subtraction are a complex subtraction of the electric field generated by the two array antennas. The considerable difference in magnitude of the two array antennas in the $30° \le \theta < 80°$ directions contributed to the main beam, whereas the small difference in magnitude in the $100° \le \theta < 140°$ directions contributed to the sidelobe. The HPBW of the su btracted radiation pattern was 39.5°, and its main lobe and sidelobe directions were 53° and 120°, respectively. The sidelobe level was −16.5 dB.

Case 3: In this case, the distance between the elements in array #1 shrinks to zero; the design parameters for array #1 is $(d_1 = 0, \beta_1 = 0)$, and those for array antenna #2 is $d_2 = \lambda/2, \beta_2 = 45°$. Array #1 can be represented by an element placed at the physical array center, doubling the magnitude of the electric field intensity. According to the far-field phase distribution of array #2, shown in Fig. 3(c), the radiation pattern subtraction was a complex summation of the electric field of array #1 (element) and array #2 (array) in the direction $0 \le \theta < 41°$, and a complex subtraction of the electric field of the array antenna from the electric field of the element in the direction $41° \le \theta < 180°$. Fig.3 (c) also shows that the HPBW of the subtracted beam was 36.9°, and its mainlobe and sidelobe directions were at 50° and 141° respectively. The sidelobe level was −11.3dB.

Case 4: The design parameters of array #1 were $(d_1 = 0, \beta_1 = 0)$. The design parameters of array #2 were reduced, compared to Case 3, to $(d_2 = 3\lambda/8, \beta_2 = 45°)$. Fig.3 (d) shows that the far-field phase of array #2 is in-phase with that of the element in every direction. The subtracted radiation pattern was achieved by subtracting the magnitude of array #2 from that of array #1. The HPBW of the subtracted radiation pattern was 38.2°, and its main lobe and sidelobe directions were 51° and 143°, respectively. The sidelobe level was −15.9 dB. It is relevant that the subtracted radiation pattern of Case 3 achieved the narrowest beamwidth of 36.9° compared to other cases.

From the above discussion, the mechanism of radiation pattern subtraction antenna that provides the narrowest beamwidth is illustrated. The proposed antenna can be considered as a phased array antenna with three elements. The optimal parameters of this antenna are amplitude and phase excitation of each element and distance between elements can be obtained from the optimization algorithm.

The sidelobe level of the subtracted radiation patterns can be controlled by modifying the phase shift (β). The HPBWs and sidelobe levels of the subtracted radiation patterns from the subtraction of the electric field of array #2 (d, β) from that of array #1 ($d_1 = 0,\ \beta_1 = 0$) (the halfwave dipole with a reflector as an element) were calculated for various

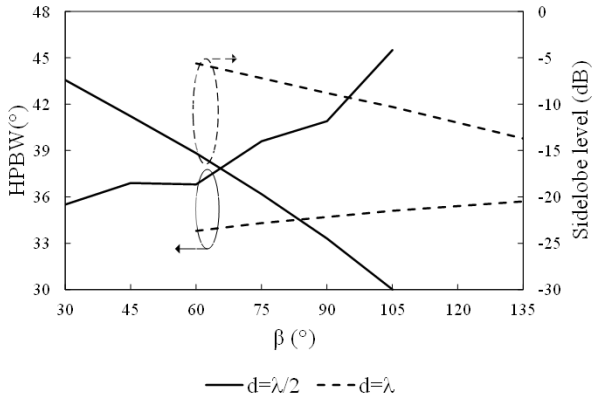

FIGURE 4. HPBW and sidelobe level of subtracted radiation patterns.

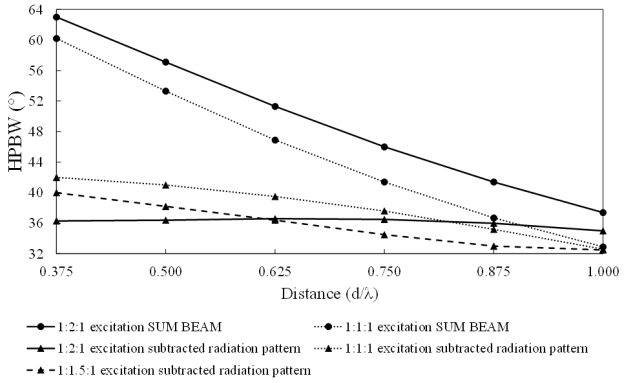

FIGURE 5. Variation of HPBW of the SUM BEAM and HPBW of radiation-pattern-subtracted antenna with varying distance d.

values of phase shift (β) and shown in Fig. 4. It can be seen that the HPBW of the radiation-pattern-subtracted antenna was narrower, while the sidelobe level increased with the decrease in phase shift (β). To achieve a narrow beamwidth with an acceptable sidelobe level, the phase shift (β) should be properly tuned for a specified distance(d). The HPBWs of the subtracted radiation pattern were calculated at the sidelobe level of -10 dB for different distances (d), as shown in Fig. 5. They were compared to the SUM BEAM of the same number of elements (three elements) and same dimensions ($d_e = d/2$). d_e is the distance between elements of the array. The effect of different excitation magnitudes is illustrated in Fig. 5.

For the SUM BEAM, its HPBWs were narrower as the distance between the elements was increased. The non-uniform excitation (1:2:1) possessed a wider beamwidth than the uniform excitation (1:1:1), as is generally known. The rate of change of HPBW of the subtracted radiation pattern was slower than that of the SUM BEAM. All HPBWs of the subtracted radiation pattern were narrower than that of the SUM BEAM for $d < 0.9\lambda$, where the 1:2:1 excitation of the subtracted radiation pattern was the widest one. The HPBWs of the 1:1:1 excitation radiation pattern subtraction and of the 1:1.5:1 excitation radiation pattern subtraction were narrower than that of the SUM BEAM.

Consider the amplitude excitation of the subtracted radiation patterns, the HPBW of the subtracted radiation pattern was almost unchanged with increasing distance (d), while the one of the SUM BEAM descreased significantly with increasing distance (d). This occurred because both the array's and the element's patterns for non-uniform excitation subtraction were much different. For $0.375 < d/\lambda < 0.625$, the HPBW changed from 1:1:1 to 1:1.5:1 and 1:2:1. The excitation of the 1:1.5:1 subtracted radiation pattern exhibited the narrowest HPBW for $d > 0.625\lambda$. In this regard, a proper separation between elements and a proper amplitude excitation had to be manually determined.

It can be seen in Fig.5 that the narrowest HPBW is 33°. A compact-sized antenna could be achieved for the case of 1:1.5:1 excitation radiation pattern subtraction. A fixed d of 0.875λ was sufficiently large to place the dipole elements in the array. Regarding the phase shift of the array, a phase shift of 70° provided a satisfactory result. Therefore, the parameters $d = 0.875\lambda$ and $\beta = 70°$ were selected for our developed antenna.

It should be noted that the 1:1.5:1 excitation subtracted radiation pattern ($d = 0.875\lambda, \beta = 70°$) provided a narrow beamwidth of 34.4° at −4.57 dB point, narrower than the 35.4° requirement stated in Section II. The maximum distance (r) from the sensor to the mango of interest was calculated by,

$$r_{\max} = d_0/\tan(\alpha_0) = 8/\tan(34.4°/2) = 26 > 25\text{cm}.$$

Therefore, the maximum antenna dimension did not exceed

$$D_{\max} = \sqrt{(\lambda \cdot r_{\max})/2} = \sqrt{(2.85 \times 26)/2} = 6.09\text{cm}.$$

IV. ANTENNA DESIGN AND EXPERIMENTAL RESULTS

This section describes the design and fabrication of the radiation pattern subtraction antenna, based on the subtraction principle presented in the previous section. CST Microwave Studio [16] was used to analyze and design the antenna. The design and analysis took into account the dielectric substrate, mutual coupling between antennas, and the type of feeding network. The halfwave-dipole element antenna structure was adopted from [17] but added a top-load structure to shorten the length of the dipole. This also reduced the mutual coupling between these elements. Therefore, the proposed antenna consisted of three top-load dipoles, a microstrip feeding circuit, and two-phase shifters. All were placed on an RG4003C substrate ($\varepsilon_r = 3.35$, $\tan\delta = 0.0027$), as can be seen in Fig. 6. The substrate was 0.508 mm thick. The copper layer was 0.035 mm thick. The metallic segments were made of copper.

Fig.6 shows three Wilkinson power combiners that provide the same input phase and a 1:1.41:1 voltage excitation (1:2:1 power excitation) to the three top-load dipoles. The HPBW of the 1:1.41:1 voltage excitation was close to that of the 1:1.5:1 voltage excitation calculated in the previous section. A phase shift of 102.8° from the feeding line II ($L_5 = 4.7$ mm) was set for dipole #3, while a phase shift of 83.7° from the feeding line I ($L_4 = 4.2$ mm) was set for dipole #1. The balanced feed of dipole #1 was configured to

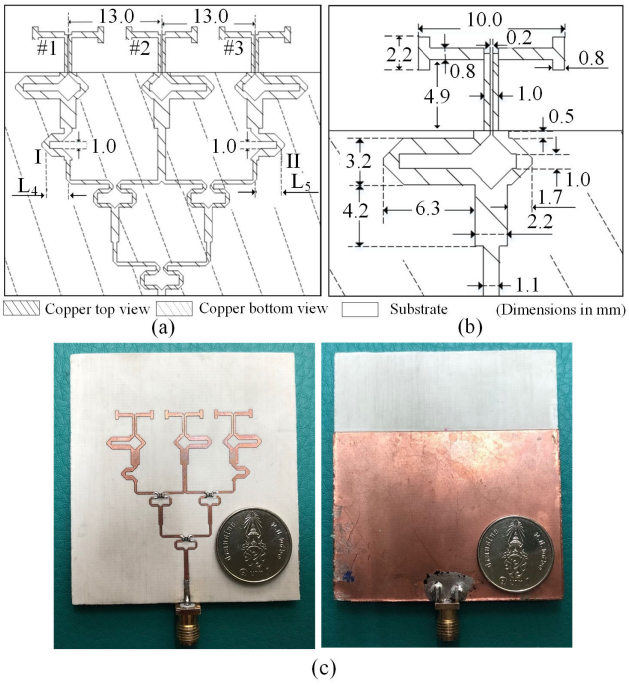

FIGURE 6. Antenna design: (a) Architecture of the radiation pattern subtraction antenna (b) Structure of the element (c) Photographs of the fabricated antenna.

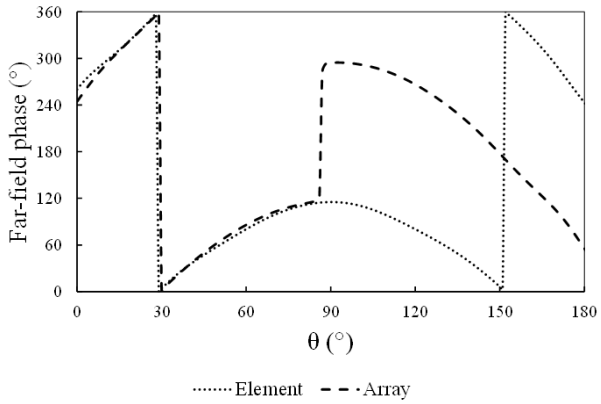

FIGURE 7. Far-field phase distribution.

be in the opposite direction to those of the other dipoles, so it already had a 180° phase difference to the other dipoles.

The dimensions of the proposed antenna that had the HPBW of 35° was 5.9 × 6.5 cm^2, which were 4.5 cm^2 smaller than the dimensions of the 1:1:1 voltage excitation SUM BEAM (6.6 × 6.5 cm^2). To represent a conventional aperture antenna, an E-plane sectoral horn with HPBW in the E-plane of 35° [15] was used. Its dimensions (length and aperture height) were 14.2 cm, and 4 cm, respectively. Hence, the proposed antenna, which had smaller dimensions, could be used at a shorter distance from the target. Furthermore, the proposed antenna was much lighter than a horn antenna. For the proposed antenna and a switched beam antenna, their dimensions were the same. However, one of the power combiners in the proposed antenna would be substituted by a phase shifter in a switched beam antenna. The benefits

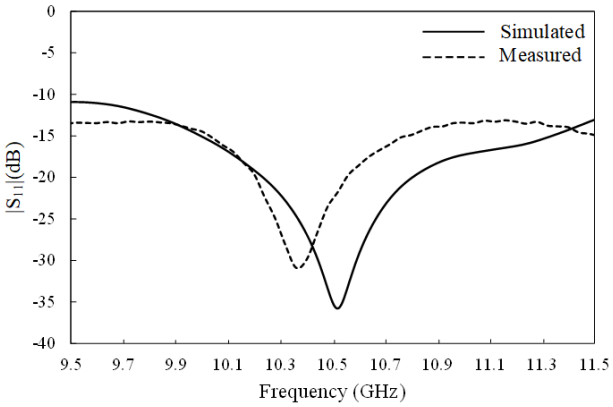

FIGURE 8. $|S_{11}|$ versus frequency.

from the proposed antenna were that memory circuit could be eliminated, and the sensor could be operated in real-time.

Our investigation of the far-field phase distribution of the top-load dipole and the array of two top-load dipoles was conducted with CST Microwave Studio. The simulated result of the far-field phase distribution of the element (top-load dipole #2) was obtained by replacing the top-load dipole #1 and #3 with two 50Ω load resistors. To determine the far-field phase distribution of the array antenna (top-load dipole #1 and #3), top-load dipole #2 was substituted with a 50Ω load resistor. In E-plane, the far-field phase distribution of the element and the array antenna were in-phase in the θ direction ($0 \leq \theta < 87°$) and almost out-of-phase in the direction ($87° \leq \theta \leq 180°$). Therefore, the subtracted radiation pattern could be obtained from a complex combination of the electric fields of the element and the array antenna in the direction ($0 \leq \theta < 87°$) and a complex subtraction of the electric fields of the element and array antenna in the direction ($87° \leq \theta \leq 180°$).

A. RADIATION-PATTERN-SUBTRACTION ANTENNA

Fig. 8 shows that, at 10.36 GHz, the proposed array antenna was well-matched with the 50Ω input, with a reflection coefficient ($|S_{11}|$) of −30.9 dB. The bandwidth of the antenna for $|S_{11}|$ less than −10 dB was around 2 GHz, from 9.5 GHz to 11.5 GHz. The slight difference in simulated and measured resonance frequencies could be from fabrication error.

Fig. 9 shows the radiation patterns in E- and H- planes of the fabricated antenna. The HPBW in the E-plane was 35°, with a main beam direction of 60°. The peak of the sidelobe was −13.5 dB below the peak of the main beam in the direction of 146°. For the H-plane at $\theta = 60°$, the main beam was in the direction of 90° with a HPBW of 100°. All of the measured results agreed very well with the simulated results of the proposed design. Any discrepancies can be attributed to the effect of the feeding structure because of slight phase shift error in fabrication.

B. ANGULAR RESOLUTION IMPROVEMENT

An improved angular resolution could be obtained more readily with a narrower beam of the subtracted radiation patterns

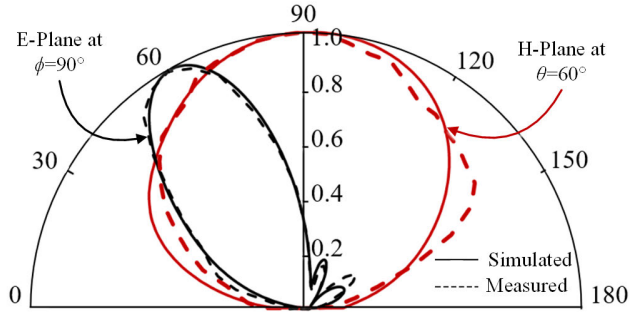

FIGURE 9. Normalized electric field patterns (a) E-plane at $\phi = 90°$ (b) H-plane at $\theta = 60°$.

(35° HPBW in E-plane) than with the broader beam of the halfwave dipole with a reflector (80° HPBW in E-plane). In our experiment, the scattered electric field intensity from the mango of interest (I) was measured with and without the influence of scattered wave from a nearby mango (N). The relative scattered electric field intensity, which is the ratio of the electric field measured from I and N and the measured electric field from only I, was calculated for several center-to-center separation distances (d_s) between I and N.

In Fig. 10 (a) and (b), the main beam direction of the sensor's antenna system was configured to point to the mango of interest (I). In the experiment, the proposed radiation-pattern-subtraction antenna was rotated 30° counter-clockwise, as could be seen in Fig. 10 (a), in order to direct the main beam toward the mango of interest. The mango of interest and the nearby mango were of average dimensions ($a = 80$ mm, $b = 150$ mm) and had almost the same dielectric properties ($\varepsilon_r = 13.7 + j8.1$ and $14.1 + j8.3$) (as measured by an Agilent 85070E Dielectric Probe Kit). The distance r between the mango of interest and the sensor's antenna system was fixed at 135 mm (from the antenna phase center to the surface of the mango). For each measurement scenario, the nearby mango was displaced from the mango of interest in the perpendicular direction to the main beam direction of the sensor's antenna with a stepping motor. Each displacement step was 10 mm. The measurement setup with the halfwave dipole with a reflector is displayed in Fig. 10 (b).

To obtain the scattered electric field intensity of the mango, three procedures were needed: Calibration, measurement of mango of interest (I), and measurement of mango of interest with the nearby mango (I +N) measurements. An Agilent FieldFox N9916A was used to measure S_{11}. In the calibration procedure, the magnitude and phase of the electric field intensity of the environment and the characteristics of the sensor's antenna were measured without any mangoes in the scene. Then, the mango of interest was placed for I measurement. Finally, for the fixed position of the mango of interest and each tested position of the nearby mango, a measurement of the magnitude and phase of the electric field intensities were made and collected. The scattered electric field intensity of the mango of interest was obtained by subtracting the respective real and imaginary parts of the calibration results

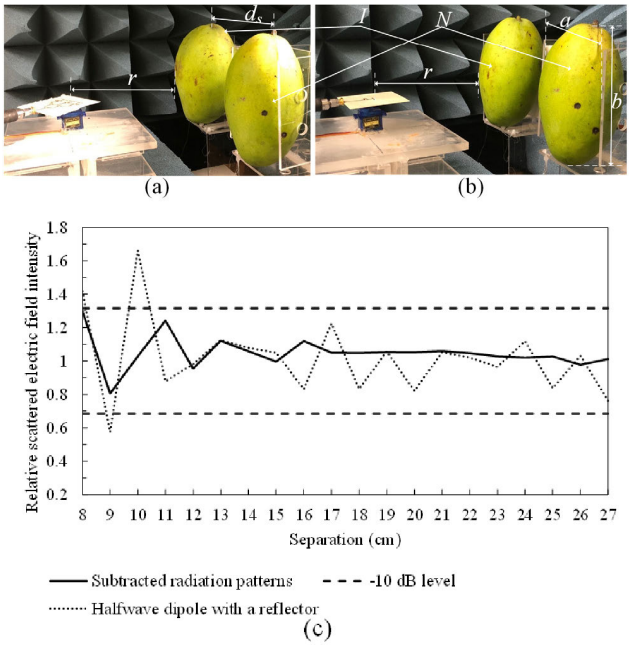

FIGURE 10. Angular resolution measurement: (a) Proposed antenna measurement setup (b) Halfwave dipole with a reflector measurement setup (c) Relative scattered electric field intensity versus separation distance.

from the real and imaginary parts of the measurement results of the mango of interest. It was, then, utilized as the reference value for clarifying the effect of the nearby mango. In the same manner, the scattered electric field intensity of the I+N was obtained.

Fig. 10 (c) shows the relative measured scattered electric field intensities of the I+N measurement for various center-to-center separation distances (d_s). The solid line represents the results from E-plane radiation-pattern subtraction antenna, while the dashed line represents the results from the halfwave dipole with a reflector. The former exhibited the effect of a narrow beam, whereas the latter exhibited the effect of a broad beam. A -10 dB point was used as the cutoff point for the effect of the nearby mango. Beyond that point, the effect can be considered negligibly small. A possible separation of 8 cm between a mango of interest and a nearby mango was indicated for the case of the E-plane subtracted radiation pattern. For the case of the halfwave dipole with a reflector, it was 10.5 cm. These results demonstrate that using radiation pattern subtraction to form a narrow beam can significantly improve angular resolution.

V. CONCLUSION

An improved-angular-resolution, the pre-harvest sensor is necessary for quality control of fruits because there can be some fruits located near the fruit of interest on a tree, and the scattered waves from them and the fruit of interest can be much different from the scattered wave from an isolated fruit of interest alone. Radiation pattern subtraction method provides angular resolution improvement, especially under the constraints that the short-distance, non-destructive sensor being light-weight and able to operate in real-time. This

article explains the idea of how a narrow beam can be accomplished by radiation pattern subtraction. Since far-field phase distribution plays a crucial role in radiation pattern subtraction, analyses of significant parameters (antenna separation and phase shift) in radiation characteristics were conducted to elucidate their influences. The proposed radiation-pattern-subtraction antenna was designed based on a top-load dipole with a reflector along with a suitable feeding network. Actual measurement results verify that this antenna, as a pre-harvest sensor, can truly mitigate the effect of nearby fruits, hence most practical for fruit-ripeness monitoring.

ACKNOWLEDGMENT

The materials for antenna fabrication were supported by ROGER corporation. We highly appreciate their support. The authors are also grateful to Mr Pratana Kangsadal, a KMITL proofreader, for kindly proofreading this manuscript.

REFERENCES

[1] *Transforming the World: The 2030 Agenda for Sustainable Development, A/RES/7-/1*, United Nations, New York, NY, USA, 2015.
[2] B. Li, J. Lecourt, and G. Bishop, "Advances in non-destructive early assessment of fruit ripeness towards defining optimal time of harvest and yield Prediction—A review," *Plants*, vol. 7, no. 1, p. 3, Jan. 2018.
[3] A. Zujevsa, V. Osadcuksa, and P. Ahrendtd, "Trends in robotic sensors technologies for fruit harvesting," *Procedia Comput. Sci.*, vol. 77, pp. 227–233, Jan. 2010.
[4] K. W. Eccleston, I. G. Platt, A. Jafari, A. Werner, C. Bateman, I. M. Woodhead, J. Fourie, J. W. H. Hsiao, and P. Carey, "Observations from radar scans of grape vines conducted over a growing season," in *Proc. IEEE Conf. Antenna Meas. Appl. (CAMA)*, Oct. 2019, pp. 1–4.
[5] M. Okada, A. Mase, and K. Uchino, "Non-destructive measurement of sugar content in apples using millimeter wave reflectometry and artificial neural networks for calibration," in *Proc. Asia–Pacific Microw. Conf.*, 2011, pp. 1386–1389.
[6] T. Tantisopharak, H. Moon, P. Youryon, K. Bunya-athichart, M. Krairiksh, and T. K. Sarkar, "Nondestructive determination of the maturity of the durian fruit in the frequency domain using the change in the natural frequency," *IEEE Trans. Antennas Propag.*, vol. 64, no. 5, pp. 1779–1787, May 2016.
[7] M. Krairiksh, J. Varith, and A. Kanjanavapastit, "Wireless sensor network for monitoring maturity stage of fruit," *Wireless Sensor Netw.*, vol. 03, no. 09, pp. 318–321, 2011.
[8] I. Skolnik, *Radar Handbook*, New York, NY, USA: McGraw-Hill, 2015.
[9] D. A. Leatherwood and E. B. Joy, "Plane wave, pattern subtraction, range compensation," *IEEE Trans. Antennas Propag.*, vol. 49, no. 12, pp. 1843–1851, Dec. 2001.
[10] A. C. Newell and G. E. Hindman, "Antenna pattern comparison using pattern subtraction and statistical analysis," in *Proc. Eur. Conf. Antennas Propag. (EuCAP)*, Rome, Italy, 2011, pp. 2537–2540.
[11] A. Agarwal, J. Reeg, A. S. Podkowa, and M. L. Oelze, "Improving spatial resolution using incoherent subtraction of receive beams having different apodizations," *IEEE Trans. Ultrason., Ferroelectr., Freq. Control*, vol. 66, no. 1, pp. 5–17, Jan. 2019.
[12] T. Sakogawa, K. Aoki, and F. Kuroki, "A technique to narrow down radiation patterns of broad beam antenna operationally and its application to security gate to prevent shoplifting based on monopulse system," in *Proc. 11th Eur. Conf. Antennas Propag. (EUCAP)*, Paris, France, Mar. 2017, pp. 1945–1948.
[13] H. N. Dao and M. Krairiksh, "A sum-difference pattern reconfigurable antenna for narrow down beamwidth of the subtracted pattern," in *Proc. IEEE-APS Topical Conf. Antennas Propag. Wireless Commun. (APWC)*, Granada, Spain, Sep. 2019, pp. 137–139.
[14] *UNECE Standard FFV-45 (Mangoes)*, United Nations, New York, NY, USA, 2017.
[15] C. A. Balanis, *Antenna Theory Analysis and Design*. Hoboken, NJ, USA: Wiley, 1997.
[16] *CST Studio Suite (User's Manual)*, 3DS Dassault Syst., Tokyo, Japan, 2019.
[17] W. R. Deal, N. Kaneda, J. Sor, Y. Qian, and T. Itoh, "A new quasi-yagi antenna for planar active antenna arrays," *IEEE Trans. Microw. Theory Techn.*, vol. 48, no. 6, pp. 910–918, Jun. 2000.

HOANG NAM DAO (Member, IEEE) was born in Bac Giang, Vietnam, in 1986. He received the B.Eng. and M.Eng. degrees from Le Quy Don Technical University, Hanoi, Vietnam, in 2010 and 2017, respectively. He is currently pursuing the D.Eng. degree with the King Mongkut's Institute of Technology Ladkrabang (KMITL), Bangkok, Thailand.

CHUWONG PHONGCHAROENPANICH (Member, IEEE) received the B.Eng. (Hons.), M.Eng., and D.Eng. degrees from the King Mongkut's Institute of Technology Ladkrabang (KMITL), Bangkok, Thailand, in 1996, 1998, and 2001, respectively. He is currently an Associate Professor with the Department of Telecommunications Engineering, KMITL, where he also serves as the Leader for the Innovative Antenna and Electromagnetic Applications Research Laboratory. His research interests include antenna design for various mobile and wireless communications, conformal antennas, and array antenna theory. He is also a member IEICE and ECTI. He served as the Chair for the IEEE MTT/AP/ED Thailand Chapter, from 2014 to 2018. He has been the organizing committee of several international conferences, including the TPC Chair of the 2009 International Symposium on Antennas and Propagation (ISAP 2009) and a TPC member of ISAP 2012. He was on the Board Committee of ECTI Association, from 2008 to 2011 and 2014 to 2015. He was the Associate Editor of *IEICE Transactions on Communications* and the *ECTI Transactions on Electrical Engineering, Electronics, and Communications*. He is also the Associate Editor of the *IEICE ComEx*. He is also a Reviewer of many scientific journals, including the IEEE Transactions on Antennas and Propagation, IEEE Access, *IET Microwaves, Antennas and Propagation*, *Electronics Letters*, *ECTI Transactions*, and many international conferences, including ISAP and APMC.

MONAI KRAIRIKSH (Senior Member, IEEE) was born in Bangkok, Thailand. He received the B.Eng., M.Eng., and D.Eng. degrees in electrical engineering from the King Mongkut's Institute of Technology Ladkrabang (KMITL), Thailand in 1981, 1984, and 1994, respectively. He was a Visiting Research Scholar with Tokai University, in 1988, and also with the Yokosuka Radio Communications Research Center, Communications Research Laboratory (CRL), in 2004. He joined KMITL, where he is currently a Professor with the Department of Telecommunication Engineering. He has served as the Director for the Research Center for Communications and Information Technology from 1997 to 2002. His current research interests include antennas for wireless communications and microwave in agricultural applications.

Dr. Krairiksh was the Chairman of the IEEE MTT/AP/Ed joint chapter in 2005 and 2006. He served as the General Chairman of the 2007 Asia-Pacific Microwave Conference and the 2017 International Symposium on Antennas and Propagation. He was the President of the Electrical Engineering/Electronics, Computer, Telecommunications and Information Technology Association (ECTI), in 2010 and 2011, and was an Editor-in-Chief of the *ECTI Transactions on Electrical Engineering, Electronics, and Communications*. He was recognized as a Senior Research Scholar of the Thailand Research Fund, in 2005 and 2008, and a Distinguished Research Scholar of the National Research Council of Thailand. He served as IEEE Antennas and Propagation Society's Distinguished Lecturer, from 2012 to 2014, an Associate Editor, from 2014 to 2019, and an AdCom Member, from 2018 to 2020.